SLAC-PUB-1827
October 1976
(T/E)

DIFFERENTIAL CROSS SECTIONS FOR THE REACTIONS $K^-p \to \bar{K}^0 n$, $K^-p \to \bar{K}^0\Delta^0$, AND $K^+p \to K^0\Delta^{++}$ AT 13 GeV/c*

G. W. Brandenburg†, R. K. Carnegie††, R. J. Cashmore‡,
M. Davier‡‡, D. W. G. S. Leith, J. A. J. Matthews§,
W. T. Meyer, P. Walden§§, and S. H. Williams

Stanford Linear Accelerator Center
Stanford University, Stanford, California 94305

ABSTRACT

Differential cross sections for the reactions $K^-p \to \bar{K}^0 n$, $K^-p \to \bar{K}^0\Delta^0$, and $K^+p \to K^0\Delta^{++}$ in the region $0.0 < |t| < 1.2$ GeV^2 are presented from a wire spark chamber spectrometer experiment performed in a 13 GeV/c separated beam. The results are based on 20,000 Δ^{++} events, 4600 Δ^0 events, and 8500 n events. The line reversed pair of Δ reactions is used to test Regge exchange degeneracy and an SU(3) sum rule. The energy dependence of all three reactions is studied by comparison with other experiments.

(Submitted to Phys. Rev. D)

*Work supported by the Energy Research and Development Administration.
Present addresses:
†Department of Physics, MIT, Cambridge, Massachusetts.
††Department of Physics, Carleton University, Ottawa, Ontario, Canada.
‡Department of Physics, Oxford University, Keble Road, Oxford, England.
‡‡Ecole Normale Superieure, Laboratoire de l'Accelerateur Lineaire, F-91 Orsay, France.
§Department of Physics, Michigan State University, East Lansing, Michigan.
§§TRIUMF, University of British Columbia, Vancouver, B. C., Canada.

I. INTRODUCTION

We present results from a high statistics wire spark chamber spectrometer experiment to measure $K^{\pm}$ reactions on hydrogen at 13 GeV/c. The reactions

$$K^+p \rightarrow K^0\Delta^{++} \qquad (1)$$

$$K^-p \rightarrow \bar{K}^0\Delta^0 \qquad (2)$$

$$K^-p \rightarrow \bar{K}^0 n \qquad (3)$$

have been measured over the momentum transfer squared interval $0.0 < |t'| < 1.2\ \mathrm{GeV}^2$. The experiment was performed in a large aperture forward spectrometer[1] located in an rf separated beam at the Stanford Linear Accelerator Center. The data sample contains 20,000 Δ^{++}, 4600 Δ^0, and 8500 n events.

Reactions (1)-(3) may be described in terms of a t-channel exchange of Regge trajectories with ρ and A_2 quantum numbers, unnatural parity exchange being forbidden by parity conservation at the meson vertex. Except for an isospin Clebsch-Gordan coefficient, reactions (1) and (2) are a line reversed pair.

Writing the Regge amplitudes as

$$A_\rho = \gamma_\rho(t)\frac{\left[e^{-i\pi\alpha_\rho(t)}-1\right]}{\sin \pi\alpha_\rho(t)}\, s^{\alpha_\rho(t)-1} \qquad (\rho \text{ exchange})$$

$$A_R = \gamma_R(t)\frac{\left[e^{-i\pi\alpha_R(t)}+1\right]}{\sin \pi\alpha_R(t)}\, s^{\alpha_R(t)-1} \qquad (A_2 \text{ exchange}),$$

where the subscript R refers to the A_2, $\gamma(t)$ is the residue function, $\alpha(t)$ is the Regge trajectory, and s is the square of the center-of-mass energy, we see that the overall phase of each amplitude is determined by the bracketed factor. These amplitudes are summed to form the amplitudes for reactions (1) and (2) as follows:

$$A_{K^+p \to K^o \Delta^{++}} = \sqrt{\frac{1}{2}}\, A_\rho + \sqrt{\frac{3}{2}}\, A_R$$

$$A_{K^-p \to \bar{K}^o \Delta^o} = \sqrt{\frac{1}{3}} \left[- \sqrt{\frac{1}{2}}\, A_\rho + \sqrt{\frac{3}{2}}\, A_R \right]$$

The assumption of weak exchange degeneracy is that $\alpha_\rho(t) = \alpha_R(t)$, which means the ρ and A_2 exchange amplitudes are 90° out of phase; hence the interference term $\mathrm{Re}(A_\rho{}^* A_R)$ is zero. Thus weak exchange degeneracy predicts

$$\frac{d\sigma}{dt}(K^+p \to K^o \Delta^{++}) = 3\,\frac{d\sigma}{dt}(K^-p \to \bar{K}^o \Delta^o)$$

Studies in the 4 - 6 GeV/c region[2] have found this prediction to be violated by as much as 50%.

Reaction (3) has been measured many times in the energy range 3 - 35 GeV/c but this experiment has more than four times the number of events of any previous experiment.[3]

The weak exchange degeneracy argument presented above also applies to reaction (3) and its line reversed reaction

$$K^+n \to K^o p \qquad (4)$$

giving a prediction that the cross sections for the two reactions should be equal. Previous experiments[4] have tested this prediction up to 6 GeV/c and found reaction (4) to have a cross section 20 - 30% larger than reaction (3), thus violating the weak exchange degeneracy prediction.

There is also an SU(3) sum rule for reactions involving ρ and A_2 exchange. Assuming the π, K and η mesons form an SU(3) octet, we have for the Δ reactions:[5]

$$\frac{d\sigma}{dt}(K^+ p \to K^o \Delta^{++}) + 3\frac{d\sigma}{dt}(K^- p \to \bar{K}^o \Delta^o) = \frac{d\sigma}{dt}(\pi^+ p \to \pi^o \Delta^{++}) + \\ + 3\frac{d\sigma}{dt}(\pi^+ p \to \eta_8 \Delta^{++}) , \tag{1}$$

where η_8 refers to the pure octet portion of the mixed η-η' system. This relation has never before been tested.

II. DATA COLLECTION

The experiment was performed in a secondary hadron beam at SLAC, where two radio-frequency separators were used to produce a kaon beam of high purity (90%, typically). A scintillation counter hodoscope at a dispersed momentum focus gave a momentum resolution of 0.3% and an x and y coordinate scintillation hodoscope 15 m upstream of the target together with four proportional chamber planes of 1-mm wire spacing located near the hydrogen target gave a spatial resolution, including the effects of multiple scattering, of ± 0.5 mrad in angle and less than 1 mm in space. Two threshold Cerenkov counters were used to identify the incident particle as π, K, or p. Typically the flux was 7 K's per 1.6 μsec SLAC pulse, or about 1000 K's/sec.

The liquid hydrogen target was 1 m long and 5 cm in diameter.

A plan view of the spectrometer is shown in Fig. 1. The heart of it is a dipole magnet of field integral of 18 Kg-m and aperture 0.6 m × 1.8 m. Four sets of magnetostrictive readout wire spark chambers were located upstream and five located downstream of the magnet. Each spark chamber consisted of two gaps with four coordinate planes, of which two had wires tilted at ± 30° to the vertical. Small polyurethane plugs were inserted in the gaps to deaden the chambers in the beam region. The upstream spark chambers measured the track over a length of 0.9 meters and the downstream over a length of 1.8 meters, resulting

in an angular resolution for tracks leaving the target of ± 0.7 mrad and a momentum resolution which depended on the momentum and was 0.5% at 3 GeV/c and 1% at 10 GeV/c. On each side of the target was a set of spark chambers and scintillation counters which subtended about 25% of the available solid angle.

The trigger, defined by the scintillation counter hodoscopes shown in Fig. 1, required two charged particles to traverse the spectrometer after originating from a $K^{\pm}$ interaction in the target. Veto scintillation counters lined the magnet to reject events in which a charged particle struck a pole piece.

The large-aperture Cerenkov counter downstream of the spectrometer consisted of eight optically distinct mirror-phototube units. The counter was filled with Freon 12 at 1.65 atm, giving π,K separation for momenta between 2.8 and 9 GeV/c. The location of the counter was optimized for identification of fast particles of the same charge as the beam. In total, 0.95×10^9 K^+ and 0.75×10^9 K^- beam particles hit the target, producing 20 million triggers.

III. DATA REDUCTION

Candidates for forward going K^0 events were selected by requiring two tracks of opposite charge to traverse the spectrometer and originate from a common vertex, not necessarily in the hydrogen target but upstream of the first set of spark chambers. Two of the three hodoscopes labeled T, HA and HB in Fig. 1 had to have signals in the associated counter, thus assuring time agreement, and the two tracks were not allowed to pass through the same element in either of the last two hodoscopes. Events with a track that was identified by the downstream Cerenkov counter as a kaon with the same charge as the beam were rejected.

If pion masses are assumed for the oppositely charged pair, it is possible to calculate both the effective mass of the two particles and their decay angle in their center-of-mass (helicity) frame. For true pion pairs, the effective mass is

independent of decay angle; for other events, the mass changes as a function of the angle. Figure 2a shows what can be expected in a scatter plot of angle versus mass, where the angle θ is measured with respect to the positive track. Vertical bands exist for the K^0 and ρ, both being true $\pi\pi$ states; curved bands are present for $K^*(890) \rightarrow K\pi$, $K^*(1420) \rightarrow K\pi$, $\Lambda \rightarrow p\pi$, and $\phi \rightarrow KK$.

Figure 2b shows 20% of our data from the K^- incident beam. All six particles (K^0, ρ, $K^*(890)$, $K^*(1420)$, Λ and ϕ) are present, although the misidentified states have been reduced in intensity by the Cerenkov requirement. The horizontal band visible in the region $-0.5 > \cos\theta > -1.0$ is due to the 9 GeV/c limit on Cerenkov identification (for $\cos\theta < -0.5$ the Cerenkov counter gives no useful information so all events have been plotted). The plot from K^+ data looks the same except that the $\bar{\Lambda}$ is suppressed. To get a sample of K^0 or $\bar{K}^0$ candidates a mass cut was placed on $.230 < M^2_{\pi\pi} < .266\ \mathrm{GeV}^2$ ($.480 < M_{\pi\pi} < .516$ GeV). The background under the K^0 was studied by looking at events in two sidebands, each half the width of K^0 cut and located on either side of the K^0 peak. Figure 2c is a scatter-plot similar to 2b but expanded to show only the K^0 region. The solid vertical lines show the K^0 cut and the dashed lines the side band cuts. Figure 2d shows the $K^0 \rightarrow \pi^+\pi^-$ decay angular distribution obtained after correcting for background events by subtracting the events in the side bands. The distribution is seen to be flat except in the extreme forward and backward directions where the experimental acceptance goes to zero.[6]

The missing mass squared was calculated for the events in the K^0 band and the result is shown in Fig. 3a and 3b. For reactions (1) and (3) the signal to background ratio is large so that a cross section could be obtained using a simple cut on the missing mass in conjunction with a t-dependent correction for the small $K-\pi$ background under the K^0. However, a more sophisticated method is needed

to extract the Δ^0 signal. The high statistics of this experiment permit a general description of the missing mass squared distribution as a function of t. The method is described below in detail and was used for all three reactions. The procedure consisted of fits with the following four components:

(a) The first component is the resolution function used to describe the neutron peak (present only in the K^- data) and to simulate the effect of experimental resolution on the other components. The function used was a sum of two Gaussian distributions.[7]

(b) The second component represented the Δ and was given by a phase space factor multiplying a p-wave Breit-Wigner[8] with a width (Γ) given by

$$\Gamma = \Gamma_0 \left(\frac{q}{q_0}\right)^3 \frac{\rho(M^2)}{\rho\left(M_0^2\right)}$$

where q is the momentum of the Δ decay products in the Δ rest frame, and q_0 its value for the central mass value, M_0. The form factor, $\rho(M^2)$, used was an empirical form of Gell-Mann and Watson,[9] $\rho(M^2) = \left[am_\pi + q^2\right]^{-1}$ with $a = 1.3$, and Γ_0 was fixed at 109 MeV. Several other forms were tried and this one was chosen because it gave both a realistic shape and a cross section for the Δ^0 near the middle of the range of all forms tried. This component was smeared by the resolution function determined in part (a) of the fit.

(c) The third component represented the $K\pi$ background under the K^0 peak, and was obtained by fitting a smooth curve to the missing mass squared distributions for events in the side bands in Fig. 2c. This background was not allowed to vary in the overall fit.

(d) The fourth component represented the K^0 background events associated either with a higher mass nucleon isobar or an upper vertex decay such as

$K^*(890) \rightarrow K^o\pi^o$. Several forms were tried,[10] but the lowest χ^2 came from a global fit in t and M^2 of the form

$$f(t, M^2) = N \frac{q}{M} \left(\frac{M^2 - M_{th}^2}{s} \right)^{1 - 2\alpha(t)} ,$$

where q is the center-of-mass momentum of the decay products from a baryon of mass M decaying into $p\pi$. M_{th} is the threshold for $p\pi$ production (1.08 GeV), s the square of the center-of-mass energy, and α has the form $\alpha(t) = \alpha_0 + \alpha_1 t$. This form was motivated by triple Regge analyses of inclusive particle production but we make no claim that it represents true physical processes, especially at these values of M^2 and s. The factor q/M is the two-body phase space and was found necessary to give good results near threshold; away from threshold it is slowly varying. The factor N is a normalization factor and when allowed to vary, was found to be constant within errors for the K^- data and nearly constant for the K^+ data, the only exception being a rise by a factor of 2 in the forward direction as t' goes from -0.1 to 0.0 GeV^2. The values of α for the K^- data were found to be $\alpha_0 = 0.5$ and $\alpha_1 = 0.84$ and for the K^+ data $\alpha_0 = -0.15$ and $\alpha_1 = 0.84$.[11] Except for the K^+ data at low t, we got excellent fits over the entire M^2 and t range of interest using only three parameters (N, α_0, and α_1) for each beam charge. In the low t region of the K^+ data it was necessary to let N increase linearly as a function of t' by a factor of 2 between $|t'| = -0.1$ and 0.0 GeV^2 to get a good fit. This background was also smeared by the resolution function.

This four-component description was used first to fit the M_X^2 distributions for all t, yielding mass positions for the nucleon and delta and the components of the narrow and wide Gaussians used to represent the resolution. The results

are shown in Fig. 3. The data were then divided into three wide t intervals, and the fit repeated to look for possible t variations in resolution or mass position. None were found. Finally the K^+ and K^- data were divided separately into 19 narrow intervals and the resolution and mass positions were fixed at the values found in the overall fit. Each t interval had typically 2000 - 3000 events in the region $0.0 < M_x^2 < 3.0\ \mathrm{GeV}^2$. The sum of the χ^2 for the fits in the 19 fine intervals was 1127 for 1117 degrees of freedom for the K^+ data and 1086 for 1095 degrees of freedom for the K^- data; both are excellent fits.

In summary, our fit to the missing mass distribution consisted of terms representing the nucleon and delta states and separate terms for non-K^o and K^o backgrounds. The K^o background depended on only three parameters, N, α_0, and α_1, and the non-K^o background was determined from the data by the side band cuts and was not permitted to vary.

Representative fits in two regions of t for each sign of beam particle are shown in Fig. 4a - 4d. It should be noted that the apparent structure in the background under the Δ^{++} is due to the $K\pi$ background term and was due primarily to the reaction,

$$K^+p \rightarrow K^+\pi^-\Delta^{++}$$

with

$$m(K^+\pi^-) \lesssim 1.5\ \mathrm{GeV}.$$

The areas under the neutron and Δ peaks gave the observed number of events, but there is some ambiguity regarding the line shape of the Δ. While it is possible to integrate the assumed Breit-Wigner shape for the Δ to a very large mass, there is no reason to claim that this gives an accurate representation of physical processes. The unavoidable non-resonant background and poor understanding of

the Δ shape at high masses make any description in this region quite arbitrary. We therefore base our cross sections only on the number of events in the region $M_\Delta^2 < 2.0\ \mathrm{GeV}^2$. (If we integrate the Breit-Wigner shape for $M_\Delta^2 < 3.0\ \mathrm{GeV}^2$, our cross sections are higher by a factor of 1.19.) Where we compare our results to other experiments, we have attempted to take a corrected value of the cross section based on a correction calculated from the resolution and Δ shape used in the other experiment.

In Fig. 5 we show the composition of the fit as a function of t' for a missing mass squared band in the region of the neutron or Δ peak. The closed circles represent the number of events of the reaction of interest, the triangles the total background (the sum of fit components c and d), and the open circles the component d background only.

The acceptance of the spectrometer was calculated by a Monte Carlo program which took account of geometrical criteria, π decay, spark chamber and trigger inefficiency, and nuclear absorption of the π's in the spectrometer. The acceptance was a smooth function of t and varied between 15% and 30% as shown by the dashed lines in Fig. 5. Weighting the results of the fit with the acceptance gave the distribution of events as a function of t. The normalization constant was calculated from the number of incident beam kaons counted and was corrected for electronics dead time, variations in target density, and vetoes from the magnet veto counters from either accidental events or delta decay products as determined from runs in which those counters were not used. An independent check on the relative K^+/K^- normalization was provided by τ decays of the beam and agreed to within 2%. The differential cross sections, $d\sigma/dt$, are given in Table 1 and Fig. 6 and 8 for the three reactions. We have plotted these cross sections as a function of $|t'| = |t - t_{min}|$ but t_{min} at this energy is so much less than our

resolution that there is no significant difference between t and t'. The errors came from the fitting process and do not include systematics, which we estimate to be 15% for reaction (1), 20% for reaction (2), and 10% for reaction (3). Also presented in Table 1 are the cross sections integrated up to $|t'| = 1.2\ \mathrm{GeV}^2$ and the slope parameters from a fit of the function $Ae^{-bt'}$ to the data in the region $.15 < |t'| < .80\ \mathrm{GeV}^2$. Because of the dip at low t' it is important to choose a t region away from the forward direction. The errors of the integrated cross sections do include the systematic errors quoted above.

The integrated cross sections are shown with the results of other experiments[12] in Fig. 7b and 10 and the slope parameters in Fig. 7a and 9.

IV. DISCUSSION OF RESULTS

1. $K^- p \rightarrow \bar{K}^0 n$

As shown in Fig. 6, the differential cross section for this reaction has a maximum near $|t'| = 0.1\ \mathrm{GeV}^2$ and a slight dip in the forward direction. This dip is generally attributed to the dominance of helicity flip amplitudes, which must turn over in the forward direction. To study the amount of helicity non-flip amplitude present, we fit a form $\frac{d\sigma}{dt} = c(a + t')\, e^{-bt'}$ to our data and found a ratio of the integrated non-flip cross section to the total cross section of 0.37 ± 0.07, indicating that although the flip amplitude dominates, the non-flip amplitude cannot be neglected.

The energy dependence of the total cross section is shown in Fig. 7b by plotting our result with a representative sampling of earlier experiments. The data follow a smooth power law as a function of p_{lab} and our result is in agreement with the other experiments.

The slope in the region $.15 < |t'| < .80\ \mathrm{GeV}^2$ is given in Fig. 7a and shows an increase from $\sim 3\ \mathrm{GeV}^{-2}$ at 4 GeV/c to $\sim 6\ \mathrm{GeV}^{-2}$ at 13 GeV/c.

Lack of statistics for reaction (4) near 13 GeV/c prevents a sensitive comparison of the line reversed reactions (3) and (4), but when we compare our data to the best available,[13] we find no significant inequality.

2. $K^+p \rightarrow K^o\Delta^{++}$, $K^-p \rightarrow \bar{K}^o\Delta^o$

In reactions (1) and (2) (in Fig. 8 - 10), we find many of the same features as in the K charge exchange reaction. Indeed, the most striking feature is the similarity of the two sets of data. This has been observed before[13] and is quite remarkable in view of the fact that although the same trajectories are being exchanged the couplings at the baryon vertex do not involve the same SU(3) multiplet. De Brion and Peschanski[14] relate this to an empirical rule of universality in impact parameter for s channel amplitudes. The primary differences between $K\Delta$ and Kn reactions are that the latter does not have as great a turnover in the forward direction and its slope in the regions $0.15 < |t'| < 0.80$ GeV^2 is slightly less steep.

An analysis of the non-flip component cannot be done because of the large errors at the lowest values of t. These large errors are due both to the large background in this region and the sensitivity of this region to the particular background parameters used.

The slopes for these two reactions, plotted in Fig. 9, also increase and the magnitude of the slope is only slightly larger than for K charge exchange.

The integrated cross sections are shown in Fig. 10 and show the same smooth power law dependence seen in reaction (3).

The prediction of weak exchange degeneracy that

$$\frac{d\sigma}{dt}(K^+p \rightarrow K^o\Delta^{++}) = 3\,\frac{d\sigma}{dt}(K^-p \rightarrow \bar{K}^o\Delta^o)$$

is tested in Fig. 11. We find the shapes of the two cross sections to be similar.

Below $|t'| \simeq 0.15$ GeV^2 the data are consistent with equal cross sections, but this may also be due to some residual background in the Δ^0. In the interval 0.15 GeV$^2 < |t'| < .60$ GeV^2 we find the ratio of the integrated cross sections to be 1.30 ± 0.16, where we have estimated the relative systematic error between the two sets of data to be 15%. The conclusion is that between $|t'| = 0.15$ GeV and $|t'| = 0.6$ GeV, the two cross sections are unequal by about 30% and thus that the prediction of weak exchange degeneracy is not satisfied.

Also shown in Fig. 11 is a comparison to the SU(3) relation given by Eq. (1). The squares in the figure represent one-half times the right-hand side of the equation. If the SU(3) relation is good, they should lie along the average of the two $K\Delta$ cross sections. The squares come from a fit of the function $f(t)\, s^{2\alpha - 2}$ to data[15] at 5, 8, and 13.1 GeV/c for fixed t, using an effective trajectory, $\alpha(t)$, which resulted from fits to $\pi^- p \to \pi^0 n$ and $\pi^- p \to \eta^0 n$.[16] The quantitative agreement with the SU(3) relation is good within errors. Better data on the pion reactions would allow a more precise comparison.

We have combined our data on reaction (1) with the corresponding data of Ref. 2b at 4 and 6 GeV/c to extract an effective Regge trajectory. At fixed t we fit the function $f(t)\, (s/s_0)^{2\alpha(t) - 2}$ to the data and got the results shown in Fig. 12. The solid line in the figure is the best straight line fit ($\chi^2 = 6.1$ for 10 degrees of freedom) and the shaded area shows the one standard deviation error. The equation for this line is $\alpha(t) = (0.458 \pm 0.020) + (1.023 \pm 0.049)t$. For comparison, the dashed line is the extrapolation of a straight line through the ρ and A_2 masses, and it gives a fair fit to the data, with a χ^2 of 15.6 for 12 degrees of freedom, but is systematically higher than the data.

V. CONCLUSIONS

We find that all three reactions (1) - (3) show a forward turnover associated with helicity flip dominance, although there appears to be some helicity non-flip amplitude present. In addition, reactions (1) and (2) disagree with the prediction of weak exchange degeneracy. Comparison with the SU(3) sum rule for $\rho - A_2$ exchange shows fair agreement. The lack of statistics for reaction (4) prevents a comparison for reactions (3) and (4). A calculation of the effective trajectory for reaction (1) gives a result in fair agreement with a trajectory through the ρ and A_2 masses. The slopes of all three reactions at 13 GeV/c are in the range 6 - 7 GeV^{-2} for the t region $0.15 < |t'| < 0.80$ GeV^2 and show a definite increase as a function of energy.

ACKNOWLEDGMENTS

We thank A. Kilert, W. Walsh, and D. McShurley for invaluable technical service, and R. Bierce for help with the programming. The staffs of the SLAC accelerator operations, experimental facilities and computer operations group performed an essential role in this experiment.

We also thank W. Dunwoodie for many useful discussions.

REFERENCES

1. G. W. Brandenburg et al., to be published.
2. (a) D. Johnson et al., Phys. Rev. D7, 2537 (1973).

   (b) J. J. Phelan et al., Phys. Lett. 61B, 483 (1976).
3. A complete list of references up to November 1973 is found in I. Ambats et al., Nucl. Phys. B77, 269 (1974). More recent references are: R. Diebold et al., Phys. Rev. Lett. 32, 904 (1974); V. N. Bolotov et al., "Investigation of $K^-p \rightarrow \bar{K}^0 n$ Charge Exchange at Momenta 25 and 35 GeV/c," Serpukov Preprint; V. N. Bolotov et al., Yadern. Fiz. 18, 1061 (in Russian) (1973); J. J. Phelan et al., op. cit.
4. R. Diebold et al., op. cit.
5. V. Barger and D. Cline, Phys. Rev. 156, 1522 (1967). Our Eq. (1) replaces the $1/2^- \rightarrow 1/2^-$ baryon vertex with $1/2^- \rightarrow 3/2^-$.
6. The high bin near $\cos\theta = 0.9$ is due to feedthrough from the Λ decays (see Fig. 2b). Notice that the Λ band crosses the K^0 band at different values of $\cos\theta$ than for the side bands. This results in a peak in the $\cos\theta$ plot near $\cos\theta = 0.9$ with correspondingly low bins on either side due to the side band subtraction. This has no effect on the cross section because the total number of K^0 events is unchanged.
7. There is need for more than one Gaussian curve since the resolution is not the same for all events. In particular, the number of spark chambers used for track fitting and the different K^0 decay angles, which result in pions with a wide range of momenta in the spectrometer, can both cause variations in resolution.
8. J. D. Jackson, Nuovo Cimento 34, 1644 (1964).
9. M. Gell-Mann and K. M. Watson, Annu. Rev. Nucl. Sci. 4, 219 (1954).

10. Some of the other forms tried included phase space, sums of polynomials and other forms inspired by triple Regge ideas. The present form was chosen because it gave the best fit and has a remarkably small number of free parameters. The resulting cross sections were intermediate in the range of results from other backgrounds, and this variation in cross sections as the background was changed was used to assign to the results an overall uncertainty due to the unknown background shape.

11. In fitting the background we chose not to place a physical interpretation on the parameter α, looking instead for the value which gave the best fit to the data. In a triple Regge description this parameter would be an effective trajectory and it is interesting that the results from the fit to the K^- data give a trajectory consistent with a $\rho - A_2$ Regge trajectory of $\alpha(t) = .47 + .89\ t$. However, the fits to the K^+ data do not fit into this scheme very well both because of the variation of N at low t and the unphysical value for α_0.

12. Other experiments plotted in Fig. 7 or 8 are:

$$\underline{K^+ p \rightarrow K^0 \Delta^{++}}$$

(a) 3.0, 3.5, and 5.0 GeV/c: M. Ferro-Luzzi et al., Nuovo Cimento 36, 1101; Y. Goldschmidt-Clermont et al., Nuovo Cimento 46, 539 (1966).

(b) 4.0 and 6.0 GeV/c: J. J. Phelan et al., op. cit.

(c) 9.0 GeV/c: V. G. Lind et al., Nucl. Phys. B14, 1 (1969).

(d) 10 GeV/c: K. W. J. Borman et al., Nucl. Phys. B28, 171 (1971).

(e) 12.0 GeV/c: V. Waluch et al., Phys. Rev. D8, 2837 (1973).

(f) 15.7 GeV/c: K. Foley et al., Phys. Rev. D9, 42 (1974).

$$\underline{K^- p \rightarrow \bar{K}^0 \Delta^0}$$

(g) 15.7 GeV/c: K. Foley et al., ibid.

$K^- n \rightarrow \bar{K}^0 \Delta^-$

(h) 3.0 GeV/c: G. Bakker et al., Nucl. Phys. B16, 53 (1969).

(i) 4.0 and 6.0 GeV/c: J. J. Phelan et al., op. cit.

(j) 4.48 GeV/c: D. D. Carmony et al., Phys. Rev. D2, 30 (1970).

(k) 5.5 GeV/c: D. Johnson et al., op. cit.

$K^- p \rightarrow \bar{K}^0 n$

(l) 3, 4, 5, and 6 GeV/c: I. Ambats et al., op. cit.

(m) 4, 5, and 6 GeV/c: J. J. Phelan et al., op. cit.

(n) 7.1, 9.5, and 12.3 GeV/c: P. Astbury et al., Phys. Lett. 23, 396 (1966).

(o) 10.7 and 15.7 GeV/c: K. Foley et al., op. cit.

(p) 14.3 GeV/c: R. J. Miller et al., Nuovo Cimento Lett. 6, 491 (1973).

(q) 24.8 and 34.6 GeV/c: V. I. Belousov et al., Phys. Lett. 43B, 76 (1973); V. N. Bolotov et al., op. cit.

13. A. Firestone et al., Phys. Rev. Lett. 25, 958 (1970).

14. J. P. de Brion and R. Peschanski, Nucl. Phys. B81, 484 (1974).

15. D. J. Schotanus et al., Nucl. Phys. B22, 45 (1970); M. Aderholz et al., Nucl. Phys. B8, 45 (1968); S. L. Kramer, Thesis, Purdue Univ. (1971).

16. See V. Barger, "Reaction Mechanisms at High Energy," Proc. of the XVII International Conference on High Energy Physics, London, 1-10 July, 1974 (Rutherford Lab., Chilton, England, 1974).

TABLE 1

$d\sigma/dt$ ($\mu b/GeV^2$)

$M_\Delta^2 < 2.0\ GeV^2$

t' (GeV^2)	$K^+p \to K^0\Delta^{++}$	$K^-p \to \bar{K}^0\Delta^0$	$K^-p \to \bar{K}^0 n$
0.0 - .02	126 ± 38	29 ± 9	123 ± 8
.02 - .04	187 ± 28	78 ± 12	164 ± 8
.04 - .06	232 ± 19	84 ± 8	155 ± 8
.06 - .08	247 ± 8	79 ± 7	154 ± 7
.08 - .10	256 ± 7	84 ± 7	154 ± 7
.10 - .12	249 ± 7	83 ± 6	148 ± 7
.12 - .14	230 ± 7	72 ± 5	124 ± 6
.14 - .16	200 ± 6	59 ± 5	116 ± 6
.16 - .18	180 ± 6	51 ± 5	106 ± 5
.18 - .20	158 ± 5	52 ± 5	85.7 ± 4.7
.20 - .24	139 ± 3	33.4 ± 2.6	73.5 ± 3.2
.24 - .28	113 ± 3	25.2 ± 2.5	62.5 ± 2.9
.28 - .32	84.7 ± 2.7	17.3 ± 2.1	46.6 ± 2.4
.32 - .36	61.3 ± 2.4	13.2 ± 2.0	33.3 ± 2.2
.36 - .40	46.1 ± 2.0	8.5 ± 1.7	30.2 ± 2.0
.4 - .5	27.7 ± 1.0	8.1 ± 0.9	18.3 ± 1.0
.5 - .6	13.3 ± 0.8	3.3 ± 0.7	10.3 ± 0.8
.6 - .8	5.2 ± 0.4	1.8 ± 0.4	4.2 ± 0.4
.8 - 1.2	1.02 ± 0.14	1.2 ± 0.2	1.4 ± 0.2
σ_{tot} (μb)	64.7 ± 9.7	19.4 ± 3.9	40.7 ± 4.1
slope (GeV^{-2}) ($.15 < \lvert t' \rvert < .80$)	6.70 ± 0.08	7.06 ± 0.34	6.06 ± 0.13

FIGURE CAPTIONS

1. Plan view of the spectrometer. C_π and C_K are the beam Cerenkov counters and the counter XY was used to keep the beam on target. The iron/scintillator detector behind the downstream Cerenkov counter and the hodoscopes and spark chambers on each side of the LH_2 target were not used in this analysis. Hodoscopes T, HA, and HB were used to assure time agreement between the event trigger and tracks found in the spark chambers.
2. A scatter plot of the cosine of the CM helicity angle vs effective mass assuming the oppositely charged pair to be a dipion state. For true dipion states $M_{\pi\pi}$ is independent of $\cos\theta_H$. Figure 2a shows the location expected from kinematics for six particles. Figure 2b is the corresponding plot for 20% of the data from the K^- beam, showing all six particles to be present. The horizontal band in the region $\cos\theta_H < -0.5$ represents the region where the negative particle has a momentum above the maximum value for Cerenkov identification. Figure 2c is the resulting K^o band and presents the K^o cuts used as well as the cuts used to study the background distribution. Figure 2d is the resulting K^o decay angular distribution when the background sample is subtracted from the K^o sample.
3. The missing mass squared distributions for all t for (a) $K^+p \rightarrow K^oX$ and (b) $K^-p \rightarrow \bar{K}^oX$. The lines show the fit described in the text and represent the following: solid, total fit; long-short dashed, neutron component; dashed, delta component; dash-dot, total background; and dotted, background component d.
4. The missing mass squared distributions for two intervals of t. (a) and (b) are for $K^+p \rightarrow K^oX$; (c) and (d) are for $K^-p \rightarrow \bar{K}^oX$. The lines represent the same fit components as in Fig. 3.

5. The t dependence of the fit composition for three slices in missing mass squared. The solid dots represent the number of events of the reaction of interest, the triangles the total background, and the open circles the polynomial background. The dashed line is the Monte Carlo generated acceptance.

6. The differential cross section for the reaction $K^-p \rightarrow \bar{K}^0 n$.

7. (a) The slope parameter for a fit of the form $Ae^{-Bt'}$ to the reaction $K^-p \rightarrow \bar{K}^0 n$. The t' region used varies slightly between experiments but is generally in the range $0.1 < |t'| < 0.6\ GeV^2$.

   (b) The integrated cross section as a function of lab momentum for the same reaction.

8. The differential cross sections for the reaction $K^+p \rightarrow K^0\Delta^{++}$ and $K^-p \rightarrow K^0\Delta^0$. Only that part of the delta with $M_\Delta^2 < 2.0\ GeV^2$ has been used. To correct for the high mass tail, these cross sections should be multiplied by 1.19.

9. The slope parameters for a fit of the form $Ae^{-Bt'}$ to the reactions $K^-p \rightarrow K^0\Delta^{++}$ and $K^-p \rightarrow \bar{K}^0\Delta^0$ or $K^-n \rightarrow \bar{K}^0\Delta^-$. The t' region varies slightly between experiments but is generally in the range $0.1 < |t'| < 0.6\ GeV^2$.

10. The integrated cross section for the delta reactions as a function of the lab momentum. We have corrected each experiment by the appropriate factor to represent only that part of the delta with $M_\Delta^2 < 2.0\ GeV^2$.

11. Comparison of the weak exchange degeneracy prediction and the SU(3) sum rule.

12. The effective trajectory resulting from a fit of the form $d\sigma/dt(t,s) = f(t)(s/s_0)^{2\alpha_{eff}(t)-2}$ to the data at 4, 6, and 13 GeV/c. The solid line is the best straight-line fit to the data and the shaded area is the one standard deviation error. The dashed line is a straight line through the ρ and A_2 masses.

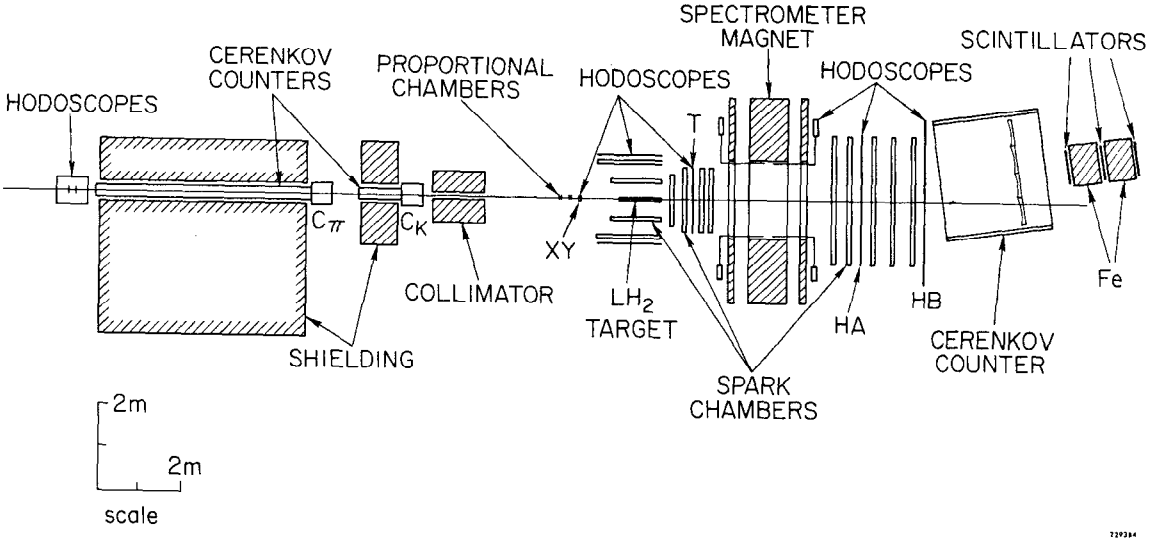
SPECTROMETER
MAGNET
SCINTILLATORS
CERENKOV
COUNTERS
PROPORTIONAL
CHAMBERS
HODOSCOPES
HODOSCOPES
HODOSCOPES
T
C_π
C_K
XY
COLLIMATOR
LH_2
TARGET
HA
HB
Fe
CERENKOV
COUNTER
SHIELDING
SPARK
CHAMBERS
2m
2m
scale

Fig. 1

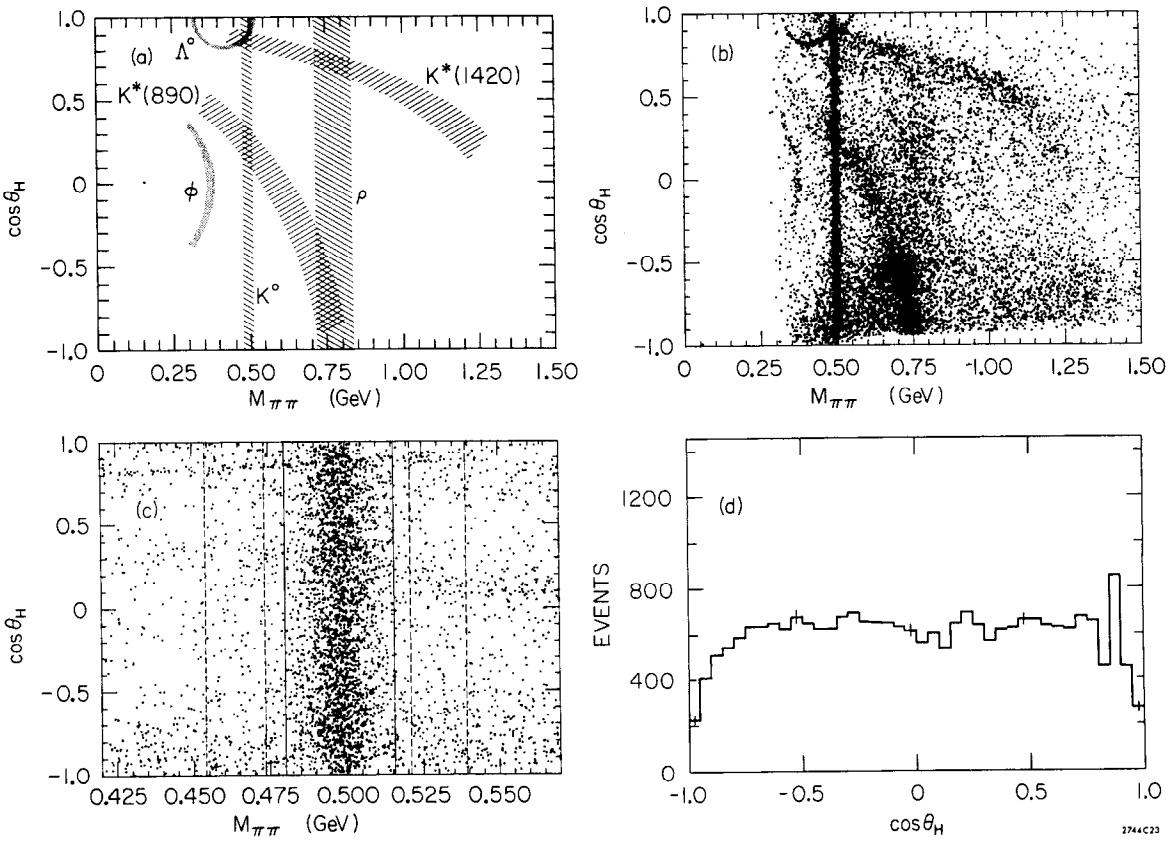

Fig. 2

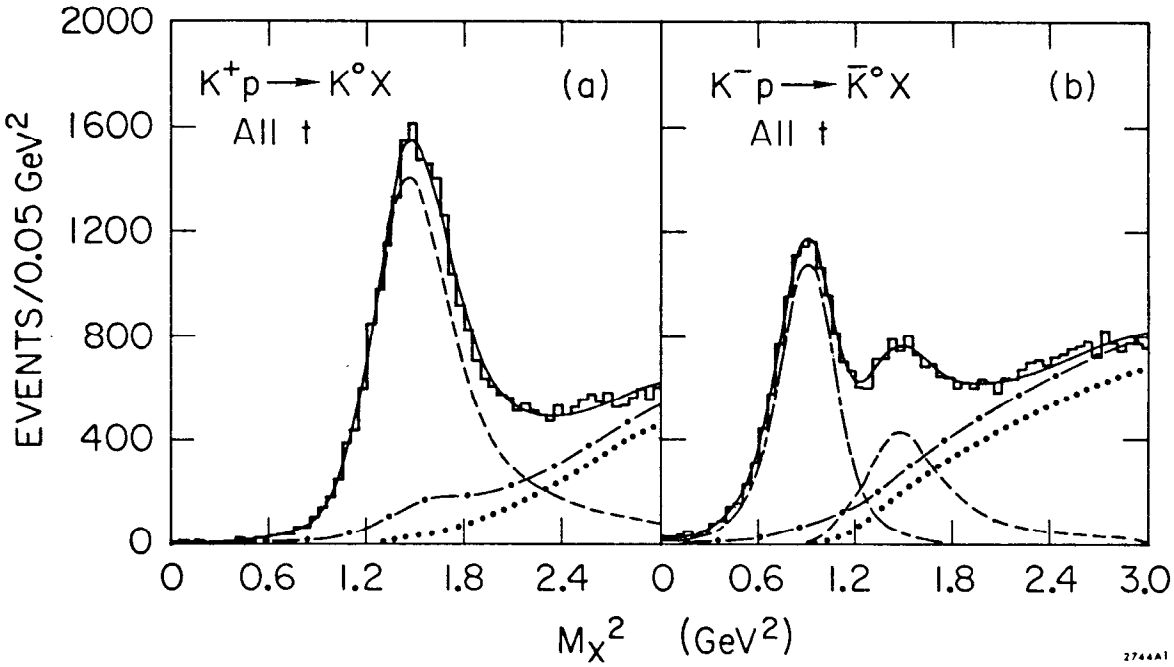
2000
1600
1200
800
400
0
EVENTS/0.05 GeV^2
$K^+p \rightarrow K^\circ X$
All t
(a)
$K^-p \rightarrow \bar{K}^\circ X$
All t
(b)
0
0.6
1.2
1.8
2.4
0
0.6
1.2
1.8
2.4
3.0
M_X^2 (GeV^2)
2744A1

Fig. 3

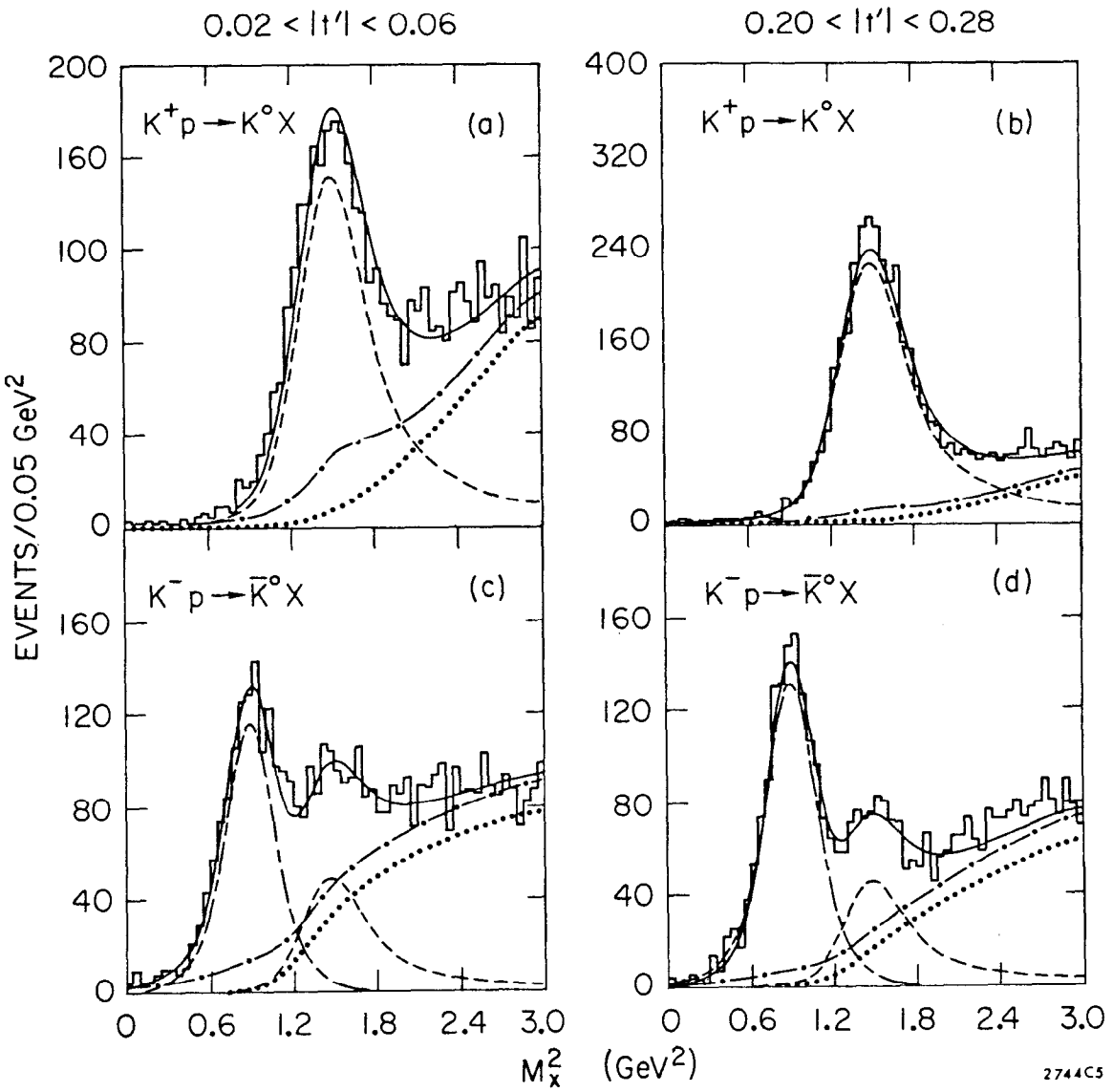
0.02 < |t'| < 0.06
0.20 < |t'| < 0.28
K+p → K°X
(a)
(b)
K−p → K̄°X
(c)
(d)
EVENTS/0.05 GeV2
M2x (GeV2)
2744C5

Fig. 4

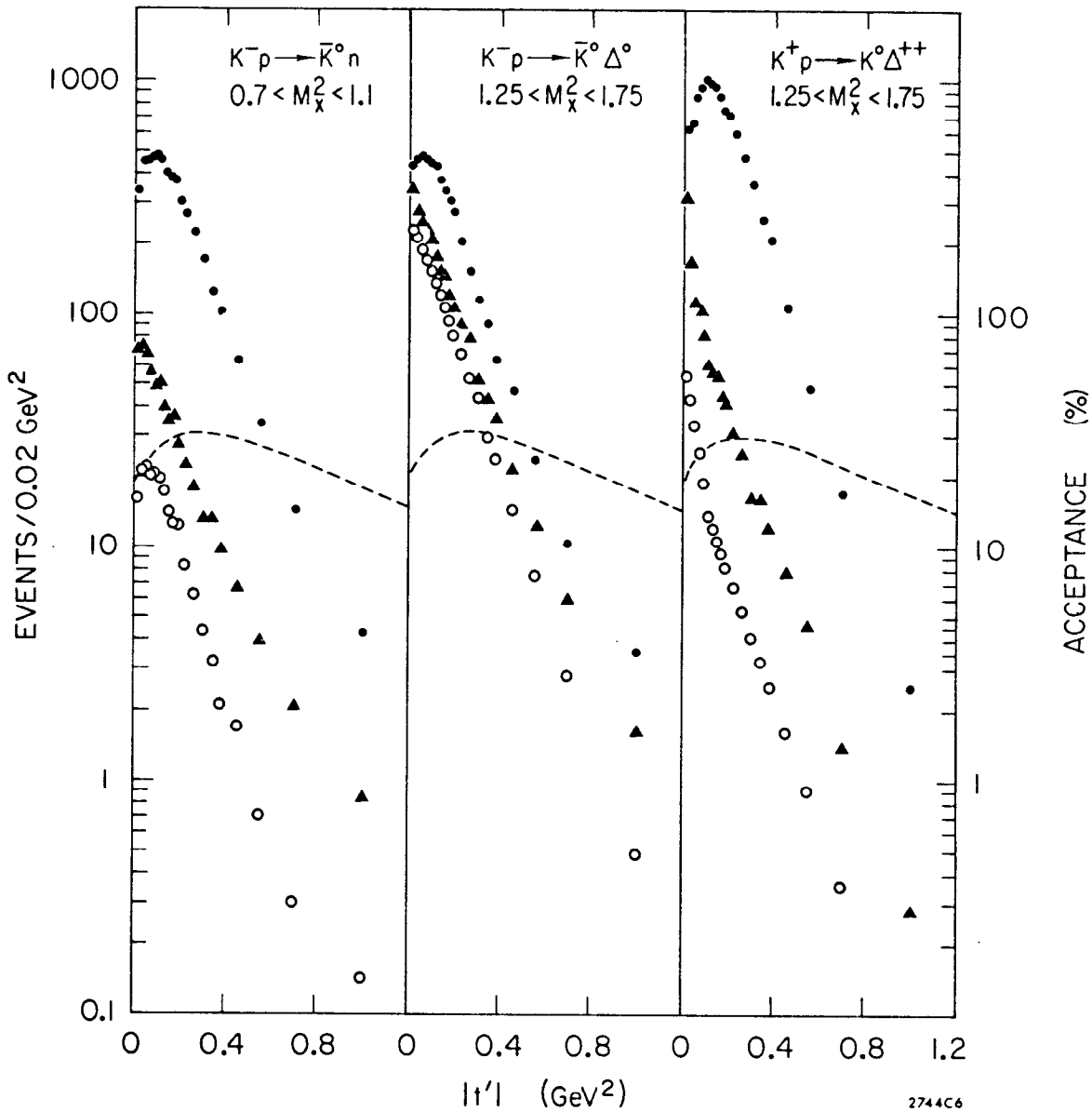
K⁻p → K̄°n
0.7 < M²x < 1.1
K⁻p → K̄° Δ°
1.25 < M²x < 1.75
K⁺p → K° Δ⁺⁺
1.25 < M²x < 1.75
EVENTS/0.02 GeV²
ACCEPTANCE (%)
|t'| (GeV²)
1000
100
10
1
0.1
0
0.4
0.8
1.2
2744C6

Fig. 5

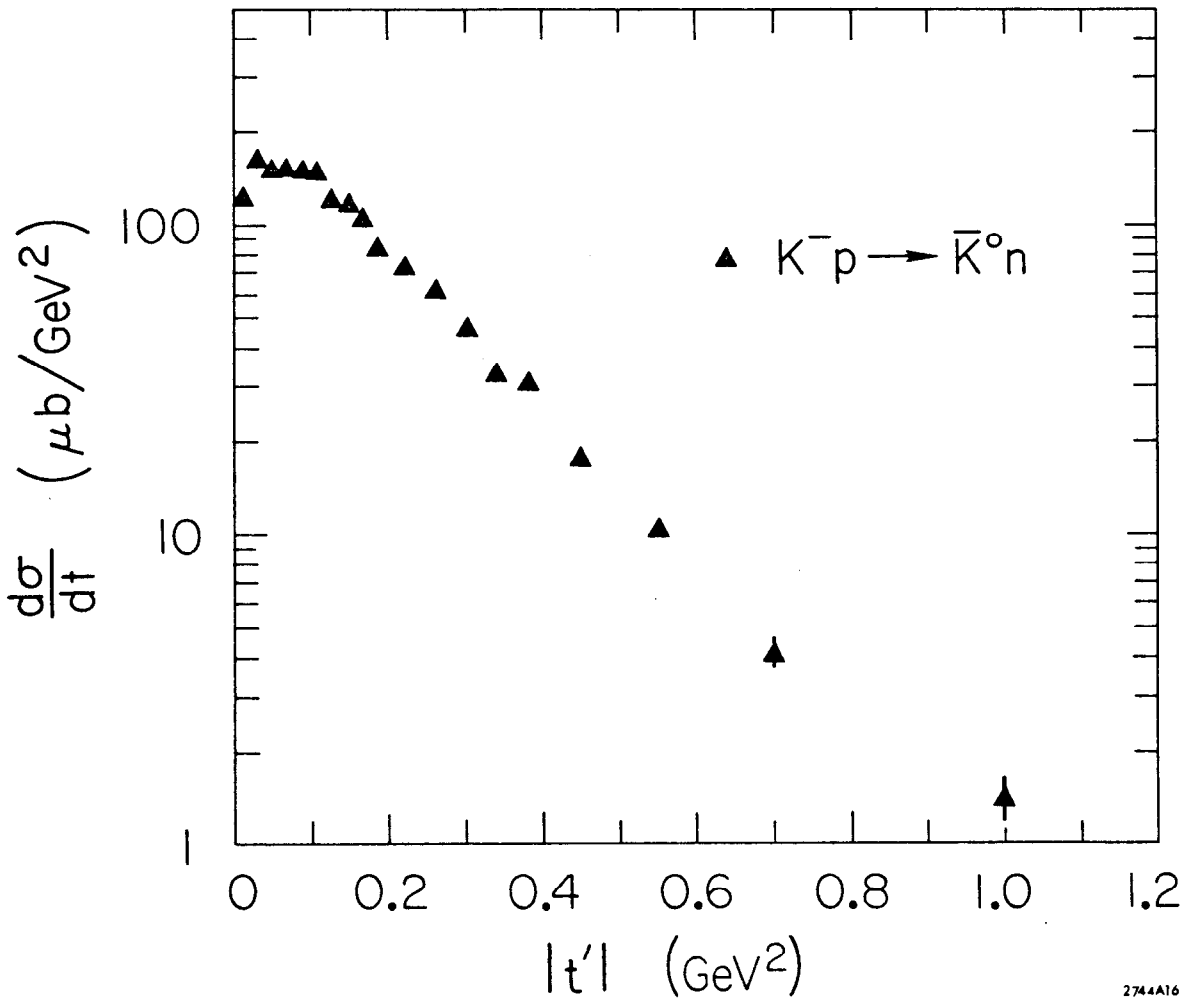
$\frac{d\sigma}{dt}$ (μb/GeV^2)
100
10
1
0
0.2
0.4
0.6
0.8
1.0
1.2
$|t'|$ (GeV^2)
$K^- p \rightarrow \bar{K}^0 n$
2744A16

Fig. 6

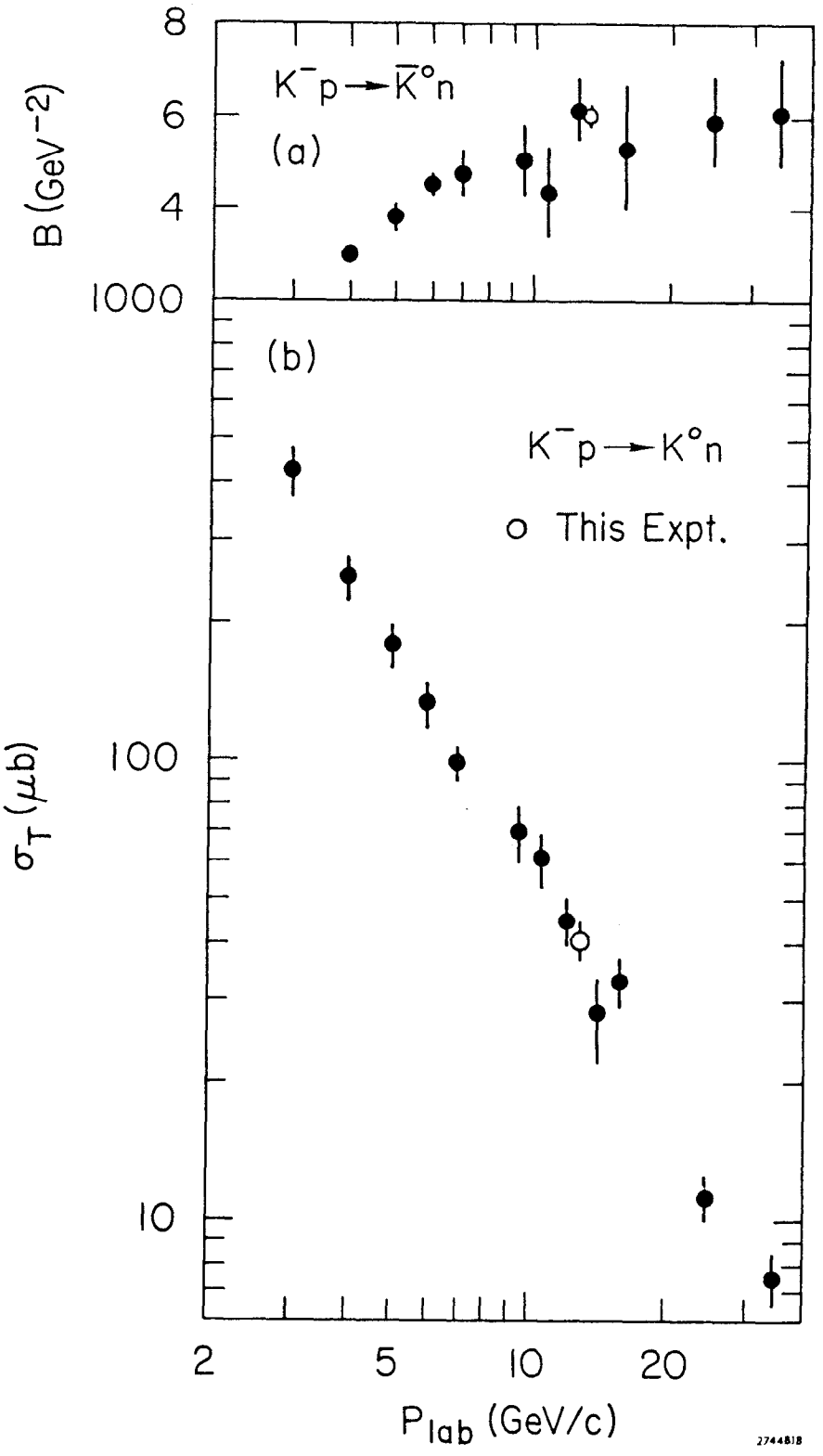
8
6
4
B (GeV^{-2})
$K^- p \rightarrow \bar{K}^0 n$
(a)
1000
100
10
σ_T (μb)
(b)
$K^- p \rightarrow K^0 n$
o This Expt.
2
5
10
20
P_{lab} (GeV/c)
2744B18

Fig 7

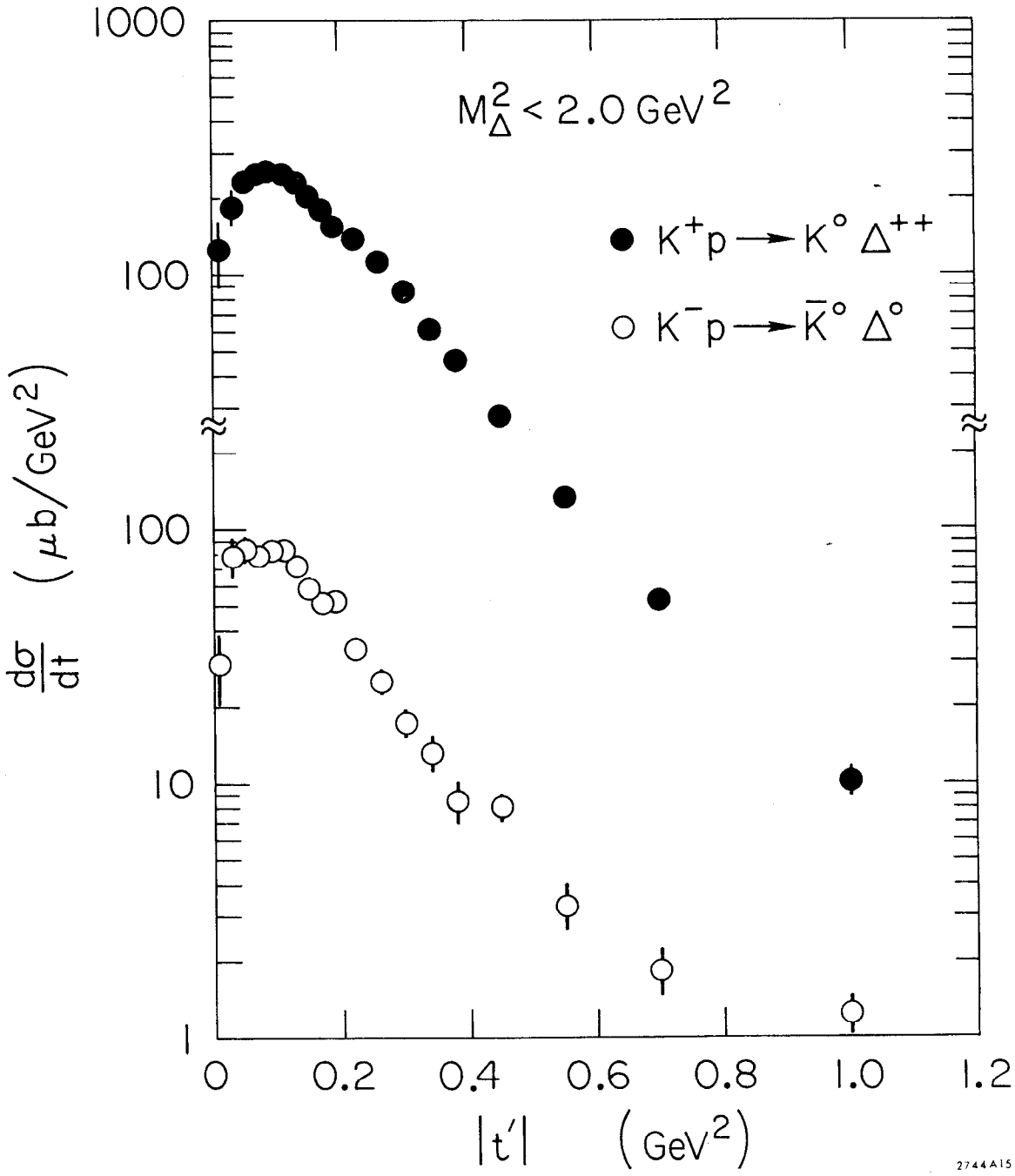
1000
100
100
10
1
$M_\Delta^2 < 2.0\ GeV^2$
$K^+p \rightarrow K^\circ \Delta^{++}$
$K^-p \rightarrow \bar{K}^\circ \Delta^\circ$
$\frac{d\sigma}{dt}$ $(\mu b/GeV^2)$
0
0.2
0.4
0.6
0.8
1.0
1.2
$|t'|$ (GeV^2)
2744A15

Fig. 8

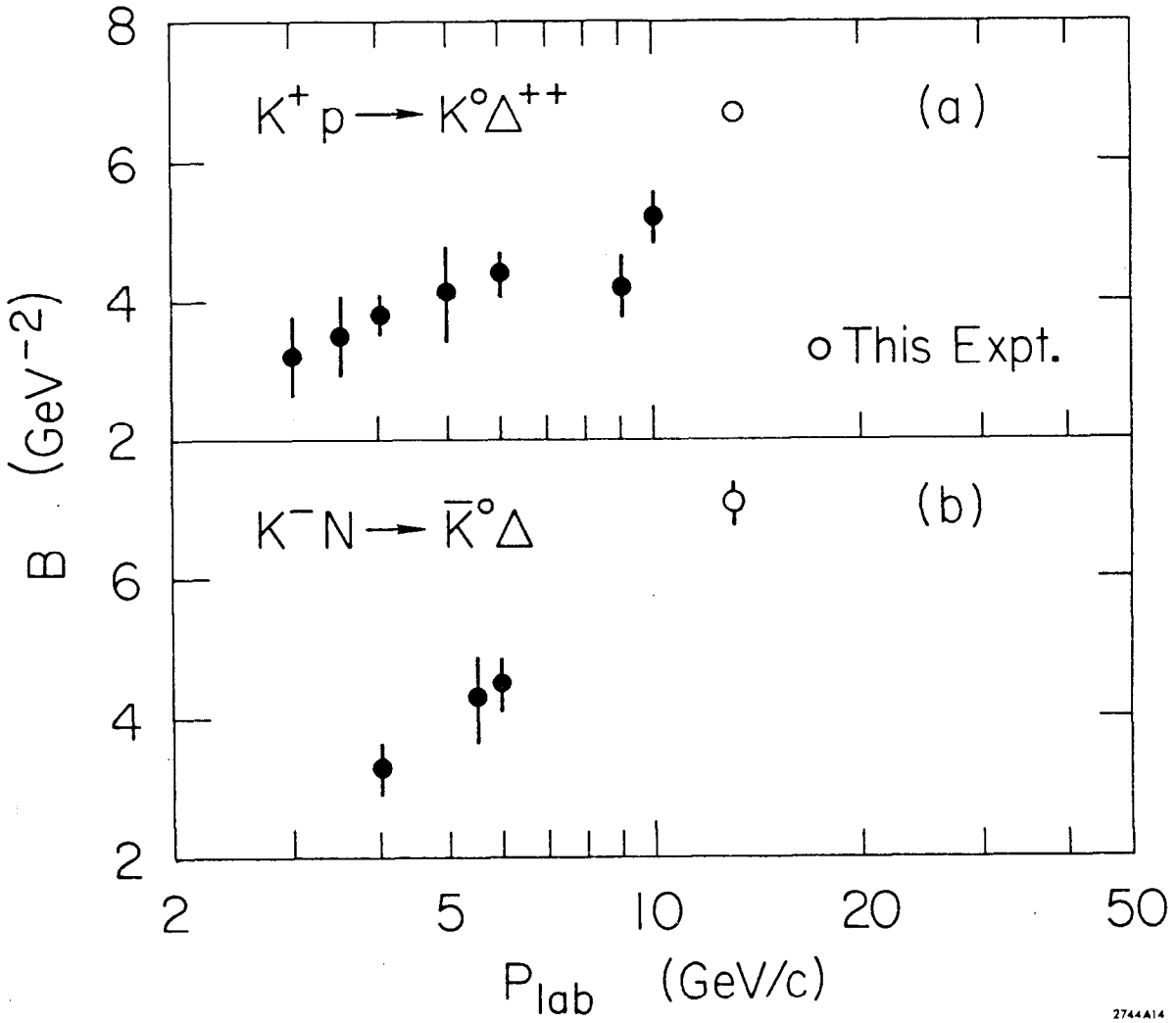
8
6
4
2
6
4
2
B (GeV^{-2})
$K^+ p \rightarrow K^\circ \Delta^{++}$
(a)
o This Expt.
$K^- N \rightarrow \bar{K}^\circ \Delta$
(b)
2
5
10
20
50
P_{lab} (GeV/c)
2744A14

Fig. 9

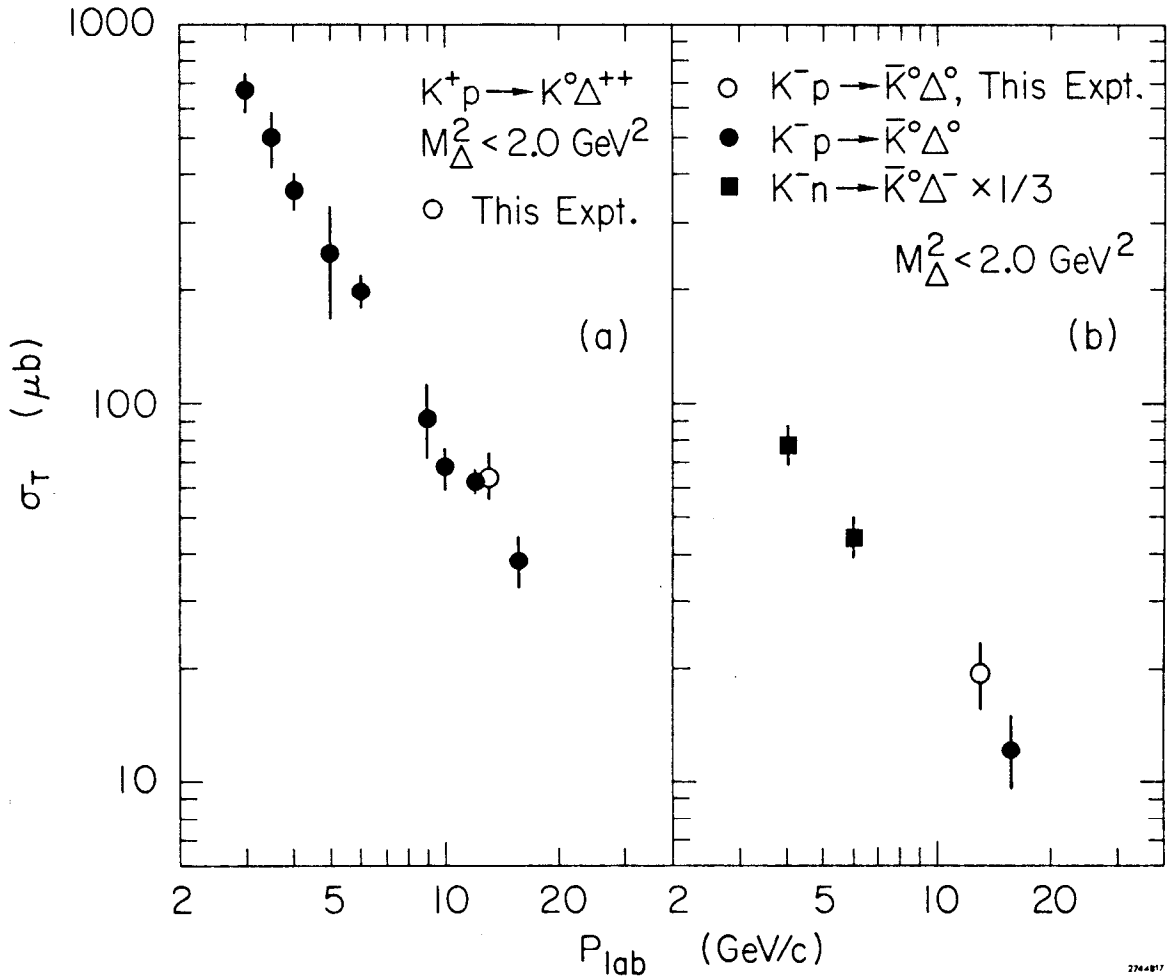
1000
100
10
σ_T (μb)
$K^+p \rightarrow K^\circ\Delta^{++}$
$M^2_\Delta < 2.0$ GeV^2
○ This Expt.
(a)
○ $K^-p \rightarrow \bar{K}^\circ\Delta^\circ$, This Expt.
● $K^-p \rightarrow \bar{K}^\circ\Delta^\circ$
■ $K^-n \rightarrow \bar{K}^\circ\Delta^- \times 1/3$
$M^2_\Delta < 2.0$ GeV^2
(b)
2
5
10
20
2
5
10
20
P_{lab} (GeV/c)

Fig. 10

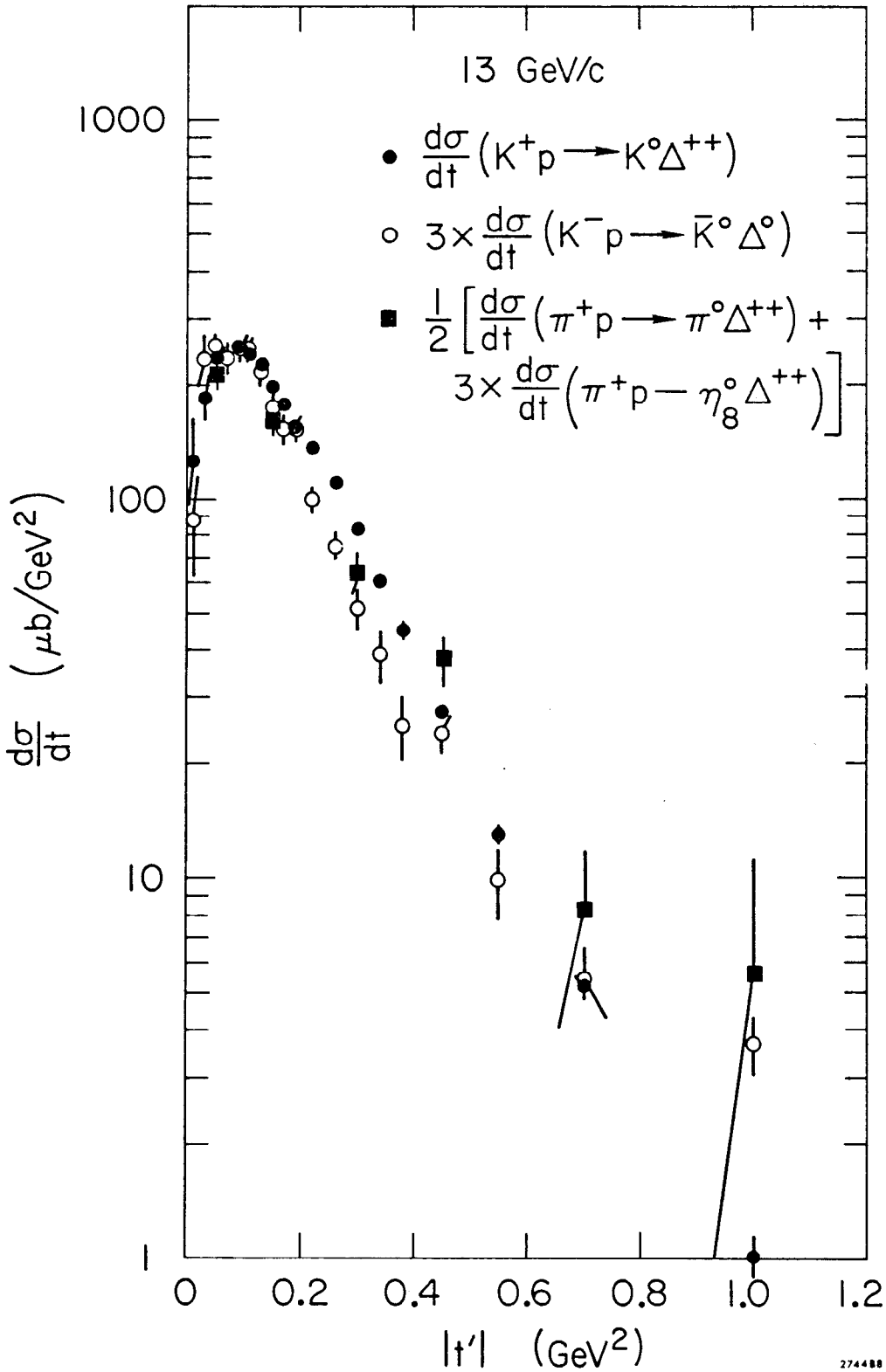
13 GeV/c
$\frac{d\sigma}{dt}(K^+p \rightarrow K^\circ\Delta^{++})$
$3\times\frac{d\sigma}{dt}(K^-p \rightarrow \bar{K}^\circ\Delta^\circ)$
$\frac{1}{2}\left[\frac{d\sigma}{dt}(\pi^+p \rightarrow \pi^\circ\Delta^{++}) + 3\times\frac{d\sigma}{dt}(\pi^+p - \eta_8^\circ\Delta^{++})\right]$
1000
100
10
1
$\frac{d\sigma}{dt}$ (μb/GeV^2)
0
0.2
0.4
0.6
0.8
1.0
1.2
$|t'|$ (GeV^2)
274488

Fig. 11

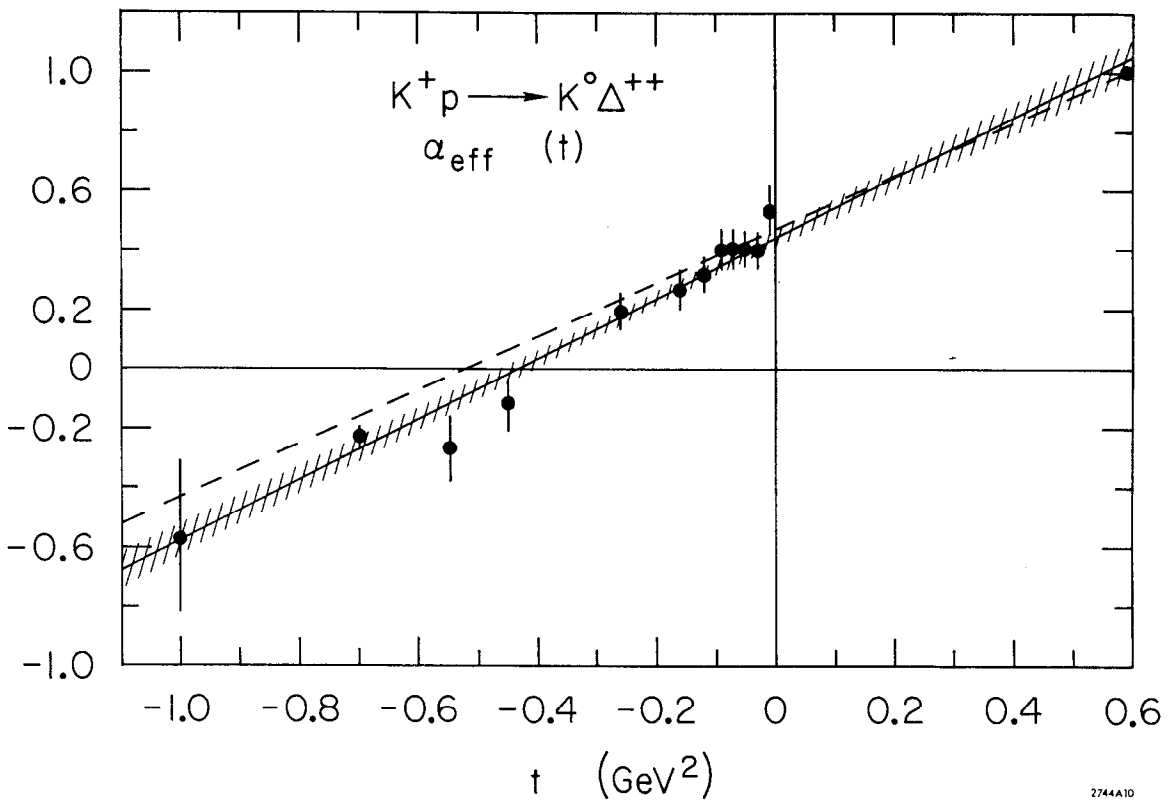
$K^+p \longrightarrow K^\circ\Delta^{++}$
α_{eff} (t)
1.0
0.6
0.2
0
-0.2
-0.6
-1.0
-1.0
-0.8
-0.6
-0.4
-0.2
0
0.2
0.4
0.6
t (GeV^2)
2744A10

Fig. 12